A poro-viscoelastic model for the subcutaneous injection of monoclonal antibodies

Yu Leng[a,*], Arezoo M. Ardekani[a], Hector Gomez[a]

[a]*School of Mechanical Engineering, Purdue University, West Lafayette, IN 47907, United States*

Abstract

Subcutaneous delivery of therapeutic monoclonal antibodies (mAbs) has recently attracted exceptional interests in the pharmaceutical industry. The mechanical response of the tissue during the injection and the drug distribution after the injection are yet to be understood. We are motivated to study the subcutaneous injection using a nonlinear poro-elastic model with a viscoelastic constitutive law of the solid. The model is first validated against experimental data of relaxation tests. Then the poro-viscoelastic model is applied to subcutaneous injection, and is compared against a poro-hyperelastic model. The pressure at the injection site, which serves as an indicator of possible fracture initiation, differs significantly by taking into account the viscosity of the solid.

Keywords: subcutaneous injection, nonlinear poro-elasticity, viscoelasticity, relaxation test, finite element method

1. Introduction

In this work, we study the numerical modeling of subcutaneous administration of monoclonal antibodies (mAbs). Therapeutic mAbs are protein-based drugs which have gained increasing attraction in the pharmaceutical industry [15]. Subcutaneous injection of mAbs is more favorable than other methods of administration, such as intravenous administration, among the patients and caregivers because it allows self-administration which reduces the expenses of healthcare [25, 30]. However, compared to intravenous administration, the short comings of the subcutaneous delivery include lower bioavalibility [41], which is the amount of drug entering the systemic circulation, and less deliverable volume [30, 48]. The study of subcutaneous injection of mAbs helps us understand the drug distribution in the subcutaneous tissue after administration and optimize delivery strategies. To accomplish that, we investigate the mechanical response, viscoelastic response more specifically, of the tissue after drug delivery using a poro-viscoelastic model.

*Corresponding author
Email address: leng10@purdue.edu (Yu Leng)

Poro-elasticity has been commonly used to model hydrated biological tissues [36, 50], such as subcutaneous tissue [33, 34, 42], brain [11, 20, 21, 44], bone [22, 45], and cartilage [19, 28]. Biphasic poro-elastic models [17, 26] assume the tissue is composed of two phases, solid and fluid. The solid phase deforms while the fluid phase is free to move in the tissue under loading conditions, such as compression, tension, shear, and injection. For small deformation, Biot's consolidation theory [4, 5, 6] is recovered from the linear poro-elastic model. The linear model is applied to subcutaneous injection in [34], but it is found in [33] that the large deformation of tissue subjected to subcutaneous injection invalidates the linear model, and it is necessary to use the nonlinear poro-elastic model to study subcutaneous delivery of mAbs for the standard flow rates ($\sim$ 0.5 mL/s). In addition, adipose tissues have exhibited viscoelastic behaviour in many experimental works [10, 39, 51, 52]. In light of these studies, we adopt the nonlinear poro-elastic model, used in [33], along with the viscoelastic constitutive law of the solid, calibrated in [10], to study the poro-elastic response of the tissue due to subcutaneous injection of mAbs.

The first motivation of this work is to validate the poro-viscoelastic model using relaxation tests reported in [10]. By simulating the relaxation test and comparing the Cauchy stress of the simulation results against experimental data, we show that the simulation results of the poro-viscoelastic model are in good agreement with the experimental records. Hence, this model is able to characterize the viscoelastic behaviour of the subcutaneous tissue. Then, the second motivation is to apply the poro-viscoelastic model to study subcutaneous injection. Using constitutive parameters identified from the relaxation tests, we compare numerical solutions of the poro-viscoelastic model with the poro-hyperelastic model, adopted in [33], and find that the pressure profiles at the injection site differ significantly for the two models.

This paper is organized as follows. In section 2, we present the model equations used in this work, including the nonlinear poro-elastic model, and the viscoelastic constitutive law of the solid. Section 3 briefly discusses the numerical methods. Then, the poro-viscoelastic model is validated using a relaxation test in section 4, and is applied to study subcutaneous injection in section 5. Finally, conclusions are summarised in section 6.

2. Model equations

We assume the injected fluid, containing a nonreactive drug (mAbs), is a Newtonian fluid, and shares the same physical properties, i.e., density and viscosity, as the interstitial fluid. The subcutaneous tissue is modeled as a biphasic material. In this section, we follow the notation of [11, 17, 18, 27] and introduce the nonlinear poro-elastic model and the viscoelastic constitutive relation of the solid.

2.1. Preliminary

We introduce first some notations, that are used throughout the paper, and the kinematics, which is also shown in fig. 1. Let $\Omega_t \subset \mathbb{R}^{\mathrm{d}}$, where $\mathrm{d} = 3$ is the

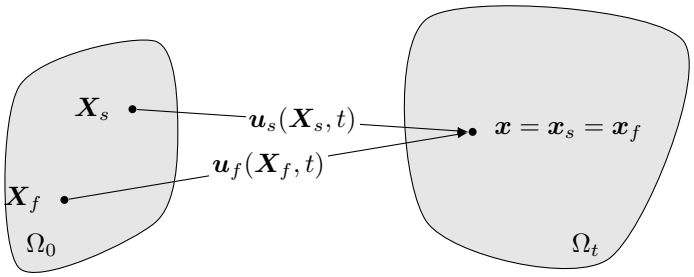

Figure 1: Schematic description of kinematics

spatial dimension, be an open, bounded, and continuously deforming domain with Lipschitz boundary $\partial\Omega_t$, for all $t \in (0, T]$, where $T > 0$. Ω_t is also called the current or deformed configuration. Following the Theory of Porous Media [11, 14, 17, 35], a spatial point $\boldsymbol{x} \in \Omega_t$ is occupied by two phases, fluid (f) and solid (s), simultaneously, i.e., $\boldsymbol{x} = \boldsymbol{x}_\alpha$, for $\alpha = s, f$. We assume the tissue is fully saturated for all $t \in (0, T]$, such that

$$\sum_{\alpha=s,f} \phi_\alpha(\boldsymbol{x}, t) = 1, \text{ in } \Omega_t, \tag{1}$$

where $\phi_\alpha(\boldsymbol{x}, t)$ is the volume fraction, defined as the volume of phase α over the total volume at $\boldsymbol{x}$ in the current configuration.

At $t = 0$, Ω_0 is referred to as the initial or undeformed configuration. The point $\boldsymbol{x}$ in the current configuration, Ω_t, is then mapped back to the initial configuration, Ω_0, at $\boldsymbol{X}_f$ and $\boldsymbol{X}_s$ for the fluid and solid phase, respectively. In general, $\boldsymbol{X}_s \neq \boldsymbol{X}_f$. The displacement field is thus defined by

$$\boldsymbol{u}_\alpha = \boldsymbol{x}_\alpha - \boldsymbol{X}_\alpha. \tag{2}$$

The deformation gradient tensor is given by

$$\boldsymbol{F}_\alpha = \frac{\partial \boldsymbol{x}_\alpha}{\partial \boldsymbol{X}_\alpha}, \tag{3}$$

where we have abused the notation $\boldsymbol{x}_\alpha$ and used it to denote the mapping from Ω_0 to Ω_t. Assuming $\boldsymbol{F}_\alpha$ is invertible for all $\boldsymbol{x}_\alpha \in \Omega_t$ and $t \in (0, T]$, we remark that the deformation gradient can also be written as

$$\boldsymbol{F}_\alpha^{-1} = \boldsymbol{I} - \nabla \boldsymbol{u}_\alpha, \tag{4}$$

where $\boldsymbol{I}$ is the d $\times$ d identity matrix, and ∇ indicates taking partial derivative with respect to $\boldsymbol{x}$ in the current configuration, Ω_t.

2.2. Nonlinear poro-elastic model

The nonlinear poro-elastic model has been used in [11, 17, 33] and we summarize the governing equations, namely, the conservation of mass and momentum equations, here for completeness. Assuming both fluid and solid phases are incompressible, we have the governing equations of a biphasic tissue as, for $t \in (0, T]$,

$$\begin{cases} \nabla \cdot \boldsymbol{\sigma}^{\text{por}} & = \mathbf{0}, \text{ in } \Omega_t, \\ \dfrac{1}{J_s}\dot{J}_s + \nabla \cdot \boldsymbol{w} & = \hat{q}_f, \text{ in } \Omega_t, \end{cases} \tag{5}$$

where $\dot{(\cdot)}$ indicates taking the material time derivative of $(\cdot)$, $\hat{q}_f$ is the fluid injection rate, $\boldsymbol{\sigma}^{\text{por}}$ is the effective Cauchy stress of the tissue, given by,

$$\boldsymbol{\sigma}^{\text{por}} = \boldsymbol{\sigma}^s_E - p\boldsymbol{I}, \tag{6}$$

with $\boldsymbol{\sigma}^s_E$ and p being the Cauchy stress of the solid phase and the pore pressure respectively, $J_s = \det(\boldsymbol{F}_s)$ is the Jacobian determinant of the solid, and $\boldsymbol{w}$ is the Darcy velocity of the fluid,

$$\boldsymbol{w} = -\frac{\boldsymbol{k}}{\mu_f}(\nabla p - \rho_f \boldsymbol{g}). \tag{7}$$

In eq. (7), $\boldsymbol{k}$ is the permeability tensor, μ_f is the fluid viscosity, ρ_f is the fluid density, and $\boldsymbol{g}$ is the body force due to gravity. It is worth noting that we have neglected the acceleration terms and body force in the equation of conservation of momentum, and have assumed the constitutive relation of the fluid flow follows Darcy's law. The fluid-solid friction can be quantified using the porous dissipation [11]

$$\mathcal{D}_v = \mu_f \left(\boldsymbol{k}^{-1}\boldsymbol{w}\right) \cdot \boldsymbol{w}. \tag{8}$$

We assume the tissue is homogeneous and isotropic, then the permeability tensor becomes $\boldsymbol{k} = k\boldsymbol{I}$, where k is the scalar permeability. The deformation of the tissue alters the pore structure of the porous medium, and the permeability changes as a consequence. To model such alternation of the permeability due to tissue deformation, we choose the normalized Kozeny-Carman formula, given by

$$k(\phi_f) = k_0 \frac{(1-\phi_{f,0}^2)^2}{\phi_{f,0}^3} \frac{\phi_f^3}{(1-\phi_f)^2}, \tag{9}$$

where $\phi_{f,0} = \phi_f(\boldsymbol{x}, 0)$ is the initial porosity, and $k_0 = k(\phi_{f,0})$ is the initial permeability. We remark that the volume fraction of the fluid (ϕ_f) in the current configuration can be found through the saturation constraint eq. (1) and the Jacobian determinant,

$$J_s \phi_s = \phi_{s,0}, \tag{10}$$

where $\phi_{s,0}$ is the initial volume fraction of the solid.

2.3. Viscoelasticity

In this subsection, our effort is resorted to find the Cauchy stress of the solid phase, $\boldsymbol{\sigma}_E^s$ in eq. (6), using the constitutive law of a viscoelastic material. Following the framework of [11], we start with the strain-energy function of a viscoelastic solid, given as

$$\Psi^s = \Psi^{\text{eq}} + \Psi^{\text{neq}}, \tag{11}$$

where Ψ^{neq} characterizes the non-equilibrium state, such as the behaviour of relaxation and creep of the solid, and Ψ^{eq} represents the equilibrium state of the solid and can be further split into two parts,

$$\Psi^{\text{eq}} = U(J_s) + \Psi^{\infty}_{\text{iso}}, \tag{12}$$

where $U(J_s)$ and $\Psi^{\infty}_{\text{iso}}$ describe the volumetric and isochoric elastic responses of the solid, respectively, as $t \to \infty$. From eq. (11), the second Piola-Kirchhoff stress, $\boldsymbol{S}_E$, can be obtained by

$$\boldsymbol{S}_E = 2\frac{\partial \Psi^s}{\partial \boldsymbol{C}_s} = 2\frac{\partial \Psi^{\text{eq}}}{\partial \boldsymbol{C}_s} + 2\frac{\partial \Psi^{\text{neq}}}{\partial \boldsymbol{C}_s} = \boldsymbol{S}^{\text{eq}} + \boldsymbol{S}^{\text{neq}}, \tag{13}$$

where $\boldsymbol{C}_s = \boldsymbol{F}_s^T \boldsymbol{F}_s$ is the right Cauchy-Green deformation tensor, $\boldsymbol{S}^{\text{neq}}$ is the non-equilibrium part of $\boldsymbol{S}_E$ and is given as

$$\boldsymbol{S}^{\text{neq}} = 2\frac{\partial \Psi^{\text{neq}}}{\partial \boldsymbol{C}_s}, \tag{14}$$

and $\boldsymbol{S}^{\text{eq}}$ is the equilibrium part of the second Piola-Kirchhoff stress and is defined by

$$\boldsymbol{S}^{\text{eq}} = 2\frac{\partial \Psi^{\text{eq}}}{\partial \boldsymbol{C}_s} = 2\frac{\partial U(J_s)}{\partial \boldsymbol{C}_s} + 2\frac{\partial \Psi^{\infty}_{\text{iso}}}{\partial \boldsymbol{C}_s} = \boldsymbol{S}^{\infty}_{\text{vol}} + \boldsymbol{S}^{\infty}_{\text{iso}}, \tag{15}$$

where $\boldsymbol{S}^{\infty}_{\text{vol}}$ and $\boldsymbol{S}^{\infty}_{\text{iso}}$ are the volumetric and isochoric contributions to $\boldsymbol{S}^{\text{eq}}$, respectively.

We adopt the extensional function given in [18] for the volumetric elastic response of the solid $U(J_s)$,

$$U_p(J_s) := \lambda(1-\phi_{s,0})^2 \left[\frac{J_s - 1}{1-\phi_{s,0}} - \ln\left(\frac{J_s - \phi_{s,0}}{1-\phi_{s,0}}\right)\right], \tag{16}$$

where λ is the first Lamé constant. For hyperelastic and viscoelastic materials without fluid, another choice of the strain energy function is given by

$$U_v(J_s) := \frac{\kappa}{4}\left(J_s^2 - 1 - 2\ln J_s\right), \tag{17}$$

where κ is the bulk modulus of the material. Because eq. (17) does not take into account the pores, we use eq. (16) for the poro-elastic models in this work.

Then, the volumetric contribution to the equilibrium second Piola-Kirchhoff stress $\boldsymbol{S}^{\text{eq}}$, eq. (15), is obtained by

$$\boldsymbol{S}^{\infty}_{\text{vol}} = 2\frac{\partial U(J_s)}{\partial \boldsymbol{C}_s} = J_s \frac{\mathrm{d}U(J_s)}{\mathrm{d}J_s}\boldsymbol{C}_s^{-1}. \tag{18}$$

For the isochoric elastic response of the tissue, we use the Ogden strain-energy function [38], which is adopted to model soft tissues in [8, 10, 11, 13, 39, 51, 53],

$$\Psi^{\infty}_{\text{iso}} = \sum_{i=1}^{3} \frac{\mu_i}{\alpha_i}\left[\overline{\lambda}_1^{\alpha_i} + \overline{\lambda}_2^{\alpha_i} + \overline{\lambda}_3^{\alpha_i} - 3\right], \tag{19}$$

where μ_i and α_i are positive constitutive parameters that are identified in experiments, $\overline{\lambda}_a$, for $a = 1, 2, 3$, is the isochoric principal stretch, which is defined by $\overline{\lambda}_a = \lambda_a J_s^{-1/3}$, where λ_a is called the principal stretch and is obtained through,

$$\boldsymbol{C}_s = \sum_{a=1}^{3} \lambda_a^2 \hat{\boldsymbol{N}}_a \otimes \hat{\boldsymbol{N}}_a. \tag{20}$$

where $\hat{\boldsymbol{N}}_a$ is the normalized eigenvector of $\boldsymbol{C}_s$, and λ_a^2 is the corresponding eigenvalue. The shear modulus can be obtained by

$$\mu = \frac{1}{2}\sum_{i=1}^{3} \mu_i \alpha_i. \tag{21}$$

The isochoric contribution to the equilibrium second Piola-Kirchhoff stress $\boldsymbol{S}^{\text{eq}}$, eq. (15), is obtained by

$$\boldsymbol{S}^{\infty}_{\text{iso}} = 2\frac{\partial \Psi^{\infty}_{\text{iso}}}{\partial \boldsymbol{C}_s} = \sum_{a=1}^{3} S_{\text{iso},a} \hat{\boldsymbol{N}}_a \otimes \hat{\boldsymbol{N}}_a, \tag{22}$$

where $S_{\text{iso},a}$ is given by

$$S_{\text{iso},a} = \frac{1}{\lambda_a}\frac{\partial \Psi^{\infty}_{\text{iso}}}{\partial \lambda_a} = \frac{1}{\lambda_a^2}\sum_{i=1}^{3} \mu_i \left[\overline{\lambda}_a^{\alpha_i} - \frac{1}{3}\left(\overline{\lambda}_1^{\alpha_i} + \overline{\lambda}_2^{\alpha_i} + \overline{\lambda}_3^{\alpha_i}\right)\right]. \tag{23}$$

The non-equilibrium part of the strain-energy function Ψ^{neq} extends the strain-energy function to the viscoelastic regime, and is responsible for the viscoelastic behaviour of the solid. The viscoelastic model is discussed in detail in [27], we present it here for completeness. Assuming the non-equilibrium state is only isochoric, we use the following form of the non-equilibrium part of the strain-energy function

$$\Psi^{\text{neq}} = \sum_{j=1}^{m} \Upsilon_j\left(\overline{\boldsymbol{C}}_s, \boldsymbol{\Gamma}_j\right), \tag{24}$$

where $\Upsilon_j, j = 1, \ldots, m$, are the so-called configurational free energy of the viscoelastic solid, m is the number of free energy terms used, $\overline{\boldsymbol{C}}_s = \overline{\boldsymbol{F}}_s^T \overline{\boldsymbol{F}}_s$ is the modified right Cauchy-Green tensor with $\overline{\boldsymbol{F}}_s = J_s^{-1/3} \boldsymbol{F}_s$ being the modified deformation gradient tensor, and $\boldsymbol{\Gamma}_j$ is the strain-like internal variable. The viscoelastic behaviour of the tissue is modeled using m viscoelastic processes with corresponding relaxation time $\tau_j > 0$, for $j = 1, \ldots, m$. Recall eq. (14), we have the non-equilibrium second Piola-Kirchhoff stress as

$$\boldsymbol{S}^{\text{neq}} = 2\frac{\partial \Psi^{\text{neq}}}{\partial \boldsymbol{C}_s} = \sum_{j=1}^{m} \boldsymbol{Q}_j, \tag{25}$$

where $\boldsymbol{Q}_j$ is the isochoric non-equilibrium stress, given by

$$\boldsymbol{Q}_j = 2\frac{\partial \Upsilon_j \left(\overline{\boldsymbol{C}}_s, \boldsymbol{\Gamma}_j\right)}{\partial \boldsymbol{C}_s}. \tag{26}$$

In order to satisfy the non-negative constraint of the internal dissipation, $\mathcal{D}_{\text{int}}$, given as

$$\mathcal{D}_{\text{int}} = -\sum_{j=1}^{m} 2\frac{\partial \Upsilon_j \left(\overline{\boldsymbol{C}}_s, \boldsymbol{\Gamma}_j\right)}{\partial \boldsymbol{\Gamma}_j} : \frac{1}{2}\dot{\boldsymbol{\Gamma}}_j \geq 0, \tag{27}$$

we choose the following equation of evolution

$$\dot{\boldsymbol{Q}}_j + \frac{\boldsymbol{Q}_j}{\tau_j} = \dot{\boldsymbol{S}}_{\text{iso},j}, \text{ for } t \in (0, T] \text{ and } j = 1, \ldots, m, \tag{28}$$

where

$$\boldsymbol{S}_{\text{iso},j} = \beta_j^{\infty} \boldsymbol{S}_{\text{iso}}^{\infty}, \tag{29}$$

for $\beta_j^{\infty} > 0$ being the dimensionless strain-energy factor. We assume the reference configuration is stress-free, namely, $\boldsymbol{Q}_j|_{t=0} = \boldsymbol{0}$. Hence, the dissipation due to the viscosity of the solid can be obtained by [27]

$$\mathcal{D}_v = \sum_{j=1}^{m} \frac{1}{\eta_j} \boldsymbol{Q}_j : \boldsymbol{Q}_j \tag{30}$$

where $\eta_j = \tau_j \beta_j^{\infty} E$, and E is the Young's modulus of the material.

Finally, by collecting the equilibrium and non-equilibrium parts, eqs. (18), (22) and (25), of the second Piola-Kirchhoff stress, $\boldsymbol{S}_E$, and pushing it forward to the current configuration, we arrive at the Cauchy stress tensor of the solid phase,

$$\boldsymbol{\sigma}_E^s = \frac{1}{J_s} \boldsymbol{F}_s \boldsymbol{S}_E \boldsymbol{F}_s^T. \tag{31}$$

Combing the nonlinear poro-elastic model, introduced in section 2.2, with the viscoelastic constitutive law of the solid, discussed in this section, we arrive at the poro-viscoelastic model.

2.4. Hyperelasticity

If the non-equilibrium contribution of the strain-energy function (Ψ^{neq}) is not considered, we arrive at the hyperelastic model which is used to model a wide range of biological tissues, such as, brain tissue [56], cervical tissue [9], subcutaneous tissue [13, 53]. The strain-energy function of the solid reduces to

$$\Psi^s = \Psi^{\text{eq}}. \tag{32}$$

As a consequence, the second Piola-Kirchhoff stress becomes

$$\boldsymbol{S}_E = 2\frac{\partial \Psi^s}{\partial \boldsymbol{C}_s} = 2\frac{\partial \Psi^{\text{eq}}}{\partial \boldsymbol{C}_s} = \boldsymbol{S}^{\text{eq}}. \tag{33}$$

By assuming Ψ^s is the same as eq. (12), we obtain $\boldsymbol{S}_E$ by gathering eqs. (18) and (22), and have the Cauchy stress tensor $\boldsymbol{\sigma}_E^s$ using the push-forward transformation, eq. (31). We remark that for the rest of the paper, we call the nonlinear poro-elastic model, as in section 2.2, along with the hyperelastic constitutive relation of the solid as the poro-hyperelastic model.

3. Numerical methods

In this section, we discuss briefly the computational procedure, such as, time integration, algorithm for the equation of evolution eq. (28), and spatial discretization used in this work. The numerical procedure is implemented using the open source finite element library `deal.II` [1, 3] and its community [11, 46, 47]. We adopt an iterative procedure namely, the fixed-stress split, to solve the nonlinear poro-elastic model, eq. (5) with appropriate boundary conditions. The fixed-stress iterative scheme for nonlinear poro-elastic models is proposed in [33] and details can be found therein.

3.1. Time integration

We use the implicit Euler scheme for time integration. Because Lagrangian mesh (introduced in section 3.3) is used, the material time derivative in the second line of eq. (5) can be approximated as

$$\dot{J}_s \approx \frac{J_s^n - J_s^{n-1}}{\Delta t}, \tag{34}$$

where we have denoted by $\Delta t = t^n - t^{n-1}$ the uniform time increment between time t^n and t^{n-1}, for $n \geq 1$, and the superscripts $(\bullet)^n$ and $(\bullet)^{n-1}$ indicate the respective values at these time instances.

3.2. Equation of evolution

In order to find the non-equilibrium stress $\boldsymbol{Q}_j$, we need to solve equation of evolution, eq. (28). The analytical solution of eq. (28) can be obtained as

$$\boldsymbol{Q}_j = e^{-t/\tau_j}\boldsymbol{Q}_j^{0^+} + \int_{0^+}^{t} e^{-(t-s)/\tau_j}\dot{\boldsymbol{S}}_{\text{iso},j}(s)\mathrm{d}s. \tag{35}$$

A time integration algorithm proposed in [27] is adopted to compute $\boldsymbol{Q}_j$. Rewriting the non-equilibrium stress at time t^n, we have

$$\begin{aligned}
\boldsymbol{Q}_j^n &= e^{-t^n/\tau_j}\boldsymbol{Q}_j^{0^+} + \int_{0^+}^{t^{n-1}} e^{-(t^n-s)/\tau_j}\dot{\boldsymbol{S}}_{\mathrm{iso},j}(s)\mathrm{d}s \\
&\qquad + \int_{t^{n-1}}^{t^n} e^{-(t^n-s)/\tau_j}\dot{\boldsymbol{S}}_{\mathrm{iso},j}(s)\mathrm{d}s \\
&= e^{-\Delta t/\tau_j}\left[e^{-t^{n-1}/\tau_j}\boldsymbol{Q}_j^{0^+} + \int_{0^+}^{t^{n-1}} e^{-(t^{n-1}-s)/\tau_j}\dot{\boldsymbol{S}}_{\mathrm{iso},j}(s)\mathrm{d}s\right] \\
&\qquad + e^{-\Delta t/(2\tau_j)}\int_{t^{n-1}}^{t^n}\dot{\boldsymbol{S}}_{\mathrm{iso},j}(s)\mathrm{d}s \\
&= e^{2\xi_j}\boldsymbol{Q}_j^{n-1} + e^{\xi_j}\beta_j^{\infty}\left[(\boldsymbol{S}_{\mathrm{iso}}^{\infty})^n - (\boldsymbol{S}_{\mathrm{iso}}^{\infty})^{n-1}\right] \\
&= e^{\xi_j}\beta_j^{\infty}(\boldsymbol{S}_{\mathrm{iso}}^{\infty})^n + e^{\xi_j}\left[e^{\xi_j}\boldsymbol{Q}_j^{n-1} - \beta_j^{\infty}(\boldsymbol{S}_{\mathrm{iso}}^{\infty})^{n-1}\right],
\end{aligned} \tag{36}$$

where from the first to the second line, we have used the mid-point rule for the third term on the right hand side, from the second to the third line, we have used eq. (29) and introduced $\xi_j = -\Delta t/(2\tau_j)$. We remark that the second term on the last line of eq. (36) can be treated as the history term of the non-equilibrium stress.

3.3. Spatial discretization

Let $\mathcal{T}_h$ be a conforming, shape-regular, quasi-uniform triangulation of the initial configuration Ω_0, consisting of polyhedrons in 3D. The finite element space for $\boldsymbol{u}_s$ is denoted as

$$\boldsymbol{V}_h := \left\{\boldsymbol{v} \in \left[H^1(\Omega_0)\right]^{\mathrm{d}} : \boldsymbol{v}|_{\Omega_e} \in \left[\mathbb{P}_1(\Omega_e)\right]^{\mathrm{d}}, \forall \Omega_e \in \mathcal{T}_h, \boldsymbol{v}|_{\Gamma_{\mathrm{D}}^{\boldsymbol{u}_s}} = \boldsymbol{0}\right\}, \tag{37}$$

where H^1 is the standard Sobolev space, $\mathbb{P}_1$ denotes linear polynomials, and $\Gamma_{\mathrm{D}}^{\boldsymbol{u}_s} \subset \partial\Omega_0$ is the Dirichlet boundary of $\boldsymbol{u}_s$. The discrete space for p is

$$\boldsymbol{Q}_h := \left\{\theta \in H^1(\Omega_0) : \theta|_{\Omega_e} \in \mathbb{P}_1(\Omega_e), \forall \Omega_e \in \mathcal{T}_h, \theta|_{\Gamma_{\mathrm{D}}^p} = 0\right\}, \tag{38}$$

where $\Gamma_{\mathrm{D}}^p \subset \partial\Omega_0$ is the Dirichlet boundary of p. Then, we obtain the fully discrete form of eq. (5): find $\boldsymbol{u}_{s,h}^n \in \boldsymbol{V}_h$, $p_h^n \in \boldsymbol{Q}_h$, such that

$$\begin{aligned}
&\int_{\Omega_t} \boldsymbol{\sigma}^{\mathrm{por}}(\boldsymbol{u}_{s,h}^n, p_h^n) : \nabla \boldsymbol{v}_h \mathrm{d}\Omega_t = 0, \quad \forall \boldsymbol{v}_h \in \boldsymbol{V}_h, \\
&\int_{\Omega_t} \frac{J_s^n - J_s^{n-1}}{J_s^n \Delta t}\theta_h \mathrm{d}\Omega_t - \int_{\Omega_t} \boldsymbol{w}^n \cdot \nabla\theta_h \mathrm{d}\Omega_t = \int_{\Omega_t} \hat{q}_f \theta_h \mathrm{d}\Omega_t, \quad \forall \theta_h \in \boldsymbol{Q}_h.
\end{aligned} \tag{39}$$

A fixed-stress split iterative scheme [33] with a tolerance of 5.0×10^{-6} is used to solve eq. (39). Such that the Conjugate Gradient solver with algebraic multigrid

preconditioner can be applied to the second equation of eq. (39), Newton's method is used to the first equation of (39). The tolerance of the nonlinear solver is taken to be 1.0×10^{-10}.

4. Model validation using relaxation test

In this section, we simulate the relaxation experiments published in [10] using the poro-viscoelastic model introduced in section 2. The experimental procedure is discussed in detail in [10], and constitutive parameters in eqs. (19) and (29) of the viscoelastic model are identified and they are independent of the strain rate.

4.1. Computational modeling of the relaxation test

In the experiments, all samples are of cylindrical shape with a diameter (Dia) of 19 mm but the height (H) varies from 5 to 10 mm. One specimen of the human adipose tissue is shown in figs. 2a and 2c. Due to symmetry, we model only a quarter of the cylindrical specimen and its computational model and mesh are shown in figs. 2b and 2d. The specimen is under unconfined uniaxial compression. The top surface of the specimen is subjected to a displacement loading (U_x) in the x direction. The loading condition is shown in fig. 3 with a strain rate of 60% s^{-1} and a final strain level of 40%. When the specimen has reached the targeted strain level (40%), the final strain is maintained for 15 minutes which is the relaxation process. The fluid is free to flow from the side of the cylinder but no flow is allowed from the top or bottom surface. The boundary conditions are summarized as follows,

$$\begin{cases} p = 0, & \boldsymbol{\sigma}^{\mathrm{por}}\boldsymbol{n} = \boldsymbol{0}, \text{ on } \sqrt{y^2+z^2} = \mathrm{Dia}/2, \\ \nabla p \cdot \boldsymbol{n} = 0, & \boldsymbol{u}_s \cdot \boldsymbol{n} = U_x(t), (\boldsymbol{\sigma}^{\mathrm{por}}\boldsymbol{n}) \cdot \boldsymbol{t} = 0, \text{ on } x = H, \\ \nabla p \cdot \boldsymbol{n} = 0, & \boldsymbol{\sigma}^{\mathrm{por}}\boldsymbol{n} = \boldsymbol{0}, \text{ on } x = 0, \\ \nabla p \cdot \boldsymbol{n} = 0, & \boldsymbol{u}_s \cdot \boldsymbol{n} = 0, (\boldsymbol{\sigma}^{\mathrm{por}}\boldsymbol{n}) \cdot \boldsymbol{t} = 0, \text{ on } y = 0, \\ \nabla p \cdot \boldsymbol{n} = 0, & \boldsymbol{u}_s \cdot \boldsymbol{n} = 0, (\boldsymbol{\sigma}^{\mathrm{por}}\boldsymbol{n}) \cdot \boldsymbol{t} = 0, \text{ on } z = 0, \end{cases} \tag{40}$$

where $\boldsymbol{n}$ and $\boldsymbol{t}$ are the unit normal and tangential vectors of the face, respectively, and $U_x(t)$ is shown in fig. 3.

A fixed mesh shown in figs. 2b and 2d is used for the simulation and the time step is $\Delta t = 0.005$ s. We remark that here and for the rest of the work, gravity is neglected, and we assume the fluid viscosity ($\mu_f = 1$ cP) is constant. The constitutive model parameters of the viscoelastic model are taken from [10, table 5] and presented in table 1. It is worth mentioning that as described in [10], 5-term ($m = 5$ as in eq. (24)) non-equilibrium forces are used and for each β_i, $i = 1, \ldots, 5$, the corresponding time constants τ_i are: $\tau_1 = 0.01$ s, $\tau_2 = 0.1$ s, $\tau_3 = 1$ s, $\tau_4 = 10$ s, and $\tau_5 = 100$ s. The permeability of the adipose tissue reported in experiments differ in several orders of magnitude ($100 - 0.01$ D) [12, 24, 32, 43, 54]; so does the porosity, which ranges from 0.01

(a) Top view of the cylindrical specimen

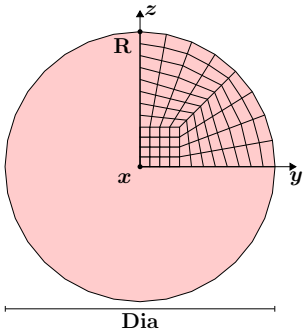

(b) Top view of the cylindrical model

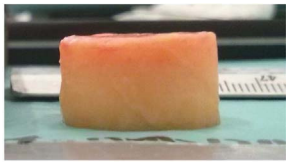

(c) Lateral view of the cylindrical specimen

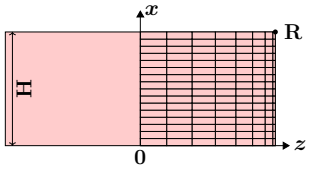

(d) Lateral view of the cylindrical model

Figure 2: One cylindrical specimen of the human adipose tissue (a and c, taken from [10]) and its computational model (b and d). The diameter (Dia in b) of the specimens is 19 mm, and the height is H (in d), where H is between 5 and 10 mm. In b, the $\boldsymbol{x}$-axis is pointing out of the paper plane.

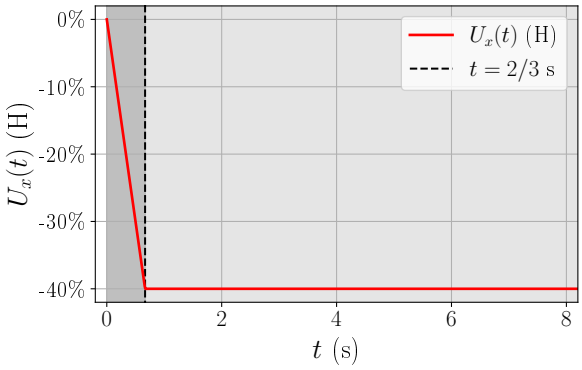

Figure 3: Displacement loading (strain rate: 60 % s^{-1}, strain level: 40 %) on the top surface of the specimen. The dark shaded area represents the loading ramp, and the light shaded area indicates the relaxation process.

to 0.23 [12, 54]. In light of these uncertainties, we choose the rest of the poroelastic model parameters as follows: the specimen height $H = 8$ mm, the initial porosity $\phi_{f,0} = 0.1$, the initial permeability $k_0 = 1$ D (D is the Darcy unit of permeability), and the Poisson ratio $\nu = 0.49$.

Table 1: Parameters identified in [10, Table 5] for the viscoelastic model with a strain rate of 60% s^{-1} and a strain level of 40%. One-term Ogden strain-energy function is used for the isochoric part of the equilibrium contribution, so $\alpha_2 = \alpha_3 = 1$, and $\mu_2 = \mu_3 = 0$. μ_1 has a unit of kPa and the rest of the parameters are dimensionless.

μ_1 (kPa)	α_1	β_1^∞	β_2^∞	β_3^∞	β_4^∞	β_5^∞
0.119	8.252	67.712	12.734	3.837	1.957	1.940

4.2. Numerical simulation of the relaxation test

The Cauchy stress on the top surface of the specimen, denoted as $\boldsymbol{T}$, can be obtained using

$$\boldsymbol{T} = \frac{1}{|S_t|} \int_{S_t} \boldsymbol{\sigma}^{\text{por}} \cdot \boldsymbol{n} \, \mathrm{d}S_t, \tag{41}$$

where S_t is the top surface ($x = H$) of the specimen, and $|S_t|$ is the measure (area) of the surface at time t. The x component, denoted as T_x, of the Cauchy stress, $\boldsymbol{T}$, is recorded and used to fit the viscoelastic model parameters in [10]. One set of the experimental data from [9] is presented in fig. 4. We use four models, i.e., hyperelastic, viscoelastic, poro-hyperelastic and poro-viscoelastic models, to simulate the relaxation test. Numerical results of T_x are shown in fig. 4.

Remark 4.1. *For the hyperelastic and viscoelastic models, we assume the displacement loading on the top surface of the specimen is quasi-static. Then we solve only the conservation of momentum without fluid pressure:*

$$\nabla \cdot \boldsymbol{\sigma}_E^s = \boldsymbol{0}. \tag{42}$$

Moreover, in the experiments [10], the adipose tissue is assumed to be incompressible, namely, $\nu = 0.5$. In fig. 4, we assume the tissue is nearly incompressible for the hyperelastic and viscoelastic models, and choose $\nu = 0.4995$. The slight compressibility is characterized using U_v defined in eq. (17) for all the simulations of the hyperelastic and viscoelastic models in this work. The boundary conditions of the hyperelastic and viscoelastic models are the same as eq. (40) without the pressure terms. The implementation of the nearly incompressible hyperelastic and viscoelastic models is nontrivial and beyond the scope of this work. We refer to [29, 40] for more details.

Figure 4 indicates that the general trends of the Cauchy stress on the top surface of the specimen from the simulation using the viscoelastic and poro-

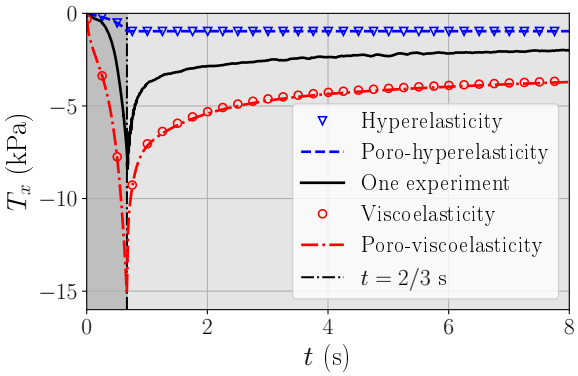

Figure 4: Cauchy stress recorded on the top surface of the specimen. The black solid line is one of the experimental records from [10]. For the hyperelastic and viscoelastic models, U_v in eq. (17) is adopted and $\nu = 0.4995$. For the poro-hyperelastic and poro-viscoelastic models, U_p in eq. (16) is adopted and $\nu = 0.49$. The dark shaded area represents the loading ramp, and the light shaded area indicates the relaxation process.

viscoelastic models agree with the experimental data. Namely, during the loading ramp, the Cauchy stress ($|T_x|$) increases with the displacement load; when the specimen is subjected to a constant displacement load at the top surface, the relaxation process starts and the Cauchy stress ($|T_x|$) decreases. The viscoelastic models are suitable to describe the relaxation behaviour of the adipose tissue. However, the hyperelastic and poro-hyperelastic models predict constant stress during the relaxation process and thus are not able to characterize the relaxation behaviour of the adipose tissue.

We remark that the experimental data presented in fig. 4 is one of 45 experiments of the same strain rate. Parameters in table 1 used for the viscoelastic model are the median values reported in fig. 4. It is expected that the stress values are different between the set of the experimental data and numerical simulations using the viscoelastic and poro-viscoelastic models. In terms of model assumptions, the viscoelastic model with $\nu = 0.4995$ is the closest match to the experiments and thus is considered the reference results.

We next justify the choice of the Poisson ratio and the volumetric strain energy function. The viscoelastic model (U_v is the strain energy function) with $\nu = 0.4995$ and 0.49, and the poro-viscoelastic model ($\nu = 0.49$) with U_v and U_p are considered. The Cauchy stress on the top surface of the specimen, the viscous dissipation defined in eq. (30) and the radial expansion (z component of the displacement, u_z) at $\mathbf{R}$ in fig. 2 are shown in figs. 5, 6a and 6b, respectively. Figure 5 shows that the Cauchy stress are similar for the two models (viscoelasticity and poro-viscoelasticity). However, as shown in fig. 6a, the viscous dissipation of the viscoelastic model is smaller for a slightly smaller Poisson ratio. For the same Poisson ratio ($\nu = 0.49$), the viscous dissipation of the poro-viscoelastic model is smaller than that of the viscoelastic model. Figure 6b indicates that if the fluid is not considered (the viscoelastic model), a smaller

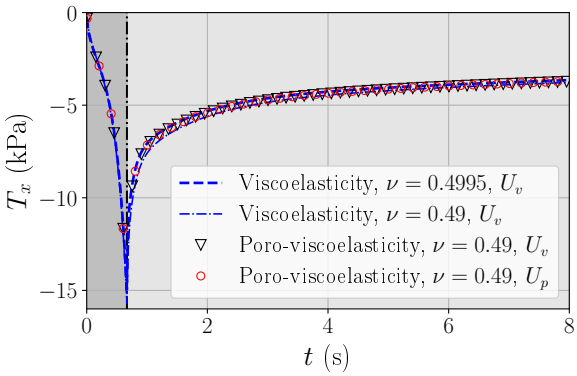

Figure 5: Cauchy stress recorded on the top surface of the specimen for different Poisson ratio and volumetric strain-energy functions. For the viscoelastic model ($\nu = 0.49$ and 0.4995), U_v (eq. (17)) is used. For the poro-viscoelastic model, $\nu = 0.49$. The dark shaded area represents the loading ramp, and the light shaded area indicates the relaxation process.

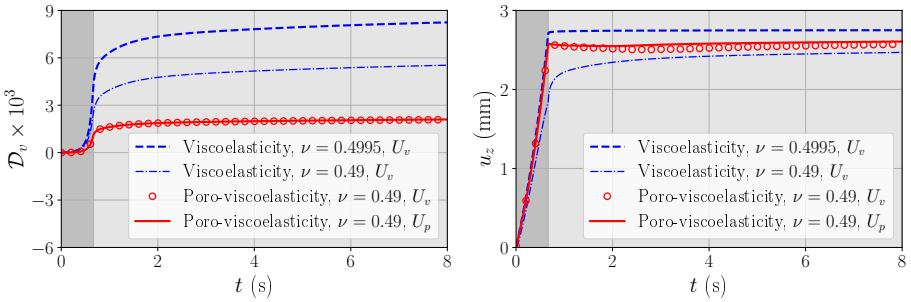

(a) Viscous dissipation (b) Displacement at **R** in fig. 2b

Figure 6: Comparison of viscous dissipation (a) and radial expansion (b) for different Poisson ratio and volumetric strain energy functions. For the viscoelastic model ($\nu = 0.49$ and 0.4995), U_v (eq. (17)) is used. For the poro-viscoelastic model, $\nu = 0.49$. The dark shaded area represents the loading ramp, and the light shaded area indicates the relaxation process.

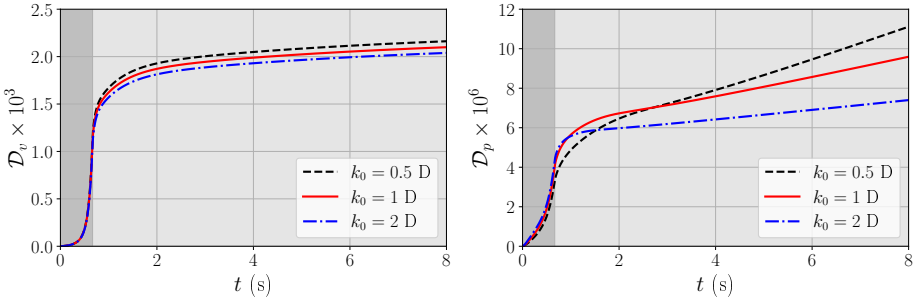

(a) Viscous dissipation (b) Porous dissipation

Figure 7: Energy dissipation due to viscous (a) and porous (b) effects of the poro-viscoelastic model for different initial permeability values, $k_0 = 0.5, 1$, and 2 D.

Poisson ratio results in less radial expansion of the tissue. For the same Poisson ratio ($\nu = 0.49$), the poro-viscoelastic model predicts slightly larger radial expansion. In addition, the difference of the numerical solution using the two volumetric strain energy functions (U_s and U_p) in the poro-viscoelastic model is negligible.

Finally, the energy dissipation due to the viscous and porous effects of the poro-viscoelastic model for three permeability values, $k_0 = 0.5, 1$, and 2 D are investigated in fig. 7. The porous dissipation shown in fig. 7b is much smaller than the viscous dissipation presented in fig. 7a. We conclude that the viscous effect is the dominating dissipation mechanism in the relaxation test and the porous effect is less significant.

5. Application to subcutaneous injection

In this section, we are motivated to study subcutaneous injection of mAbs using the poro-viscoelastic model with constitutive parameters validated in the previous section. We first briefly introduce the computational framework developed in [33]. Then we compare the numerical simulations of the poro-viscoelastic and poro-hyperelastic models using the constitutive parameters from table 1 as the viscoelastic model parameters are independent of the strain rate [10].

5.1. Computational modeling of subcutaneous injection

We briefly discuss the computational modeling of the subcutaneous tissue and injection here for completeness. We model the tissue as a three-dimensional rectangular prism, and the injection as a volumetric source located on the centerline of the tissue about 4 mm underneath the skin surface. Due to symmetry, simulations are conducted on a quarter of the prism, and the computation domain is of dimension $100 \times 100 \times 100$ mm^3 as shown in fig. 8. The mesh is adaptively refined (6 levels) near the injection site and does not change throughout the simulation. The size of the smallest element is 0.15625^3 mm^3 so that it represents the inner diameter of the needle used for subcutaneous injection (0.15 - 0.25 mm) [55]. The boundary conditions are summarized in eq. (43).

$$\begin{cases} \nabla p \cdot \boldsymbol{n} = 0, & \boldsymbol{u}_s \cdot \boldsymbol{n} = 0, (\boldsymbol{\sigma}^{\text{por}} \boldsymbol{n}) \cdot \boldsymbol{t} = 0, \text{ on } x = 0, \\ p = 0, & \boldsymbol{\sigma}^{\text{por}} \boldsymbol{n} = \boldsymbol{0}, \text{ on } x = 0.1 \text{ m}, \\ \nabla p \cdot \boldsymbol{n} = 0, & \boldsymbol{u}_s \cdot \boldsymbol{n} = 0, (\boldsymbol{\sigma}^{\text{por}} \boldsymbol{n}) \cdot \boldsymbol{t} = \boldsymbol{0}, \text{ on } y = 0, \\ p = 0, & \boldsymbol{\sigma}^{\text{por}} \boldsymbol{n} = \boldsymbol{0}, \text{ on } y = 0.1 \text{ m}, \\ p = 0, & \boldsymbol{u}_s = \boldsymbol{0}, \text{ on } z = 0, \\ \nabla p \cdot \boldsymbol{n} = 0, & \boldsymbol{\sigma}^{\text{por}} \boldsymbol{n} = \boldsymbol{0}, \text{ on } z = 0.1 \text{ m}. \end{cases} \tag{43}$$

The injection term $\hat{q}_f$ in eq. (5) is defined in the current configuration, which makes it difficult to track the injected volume. We redefine the injection in the

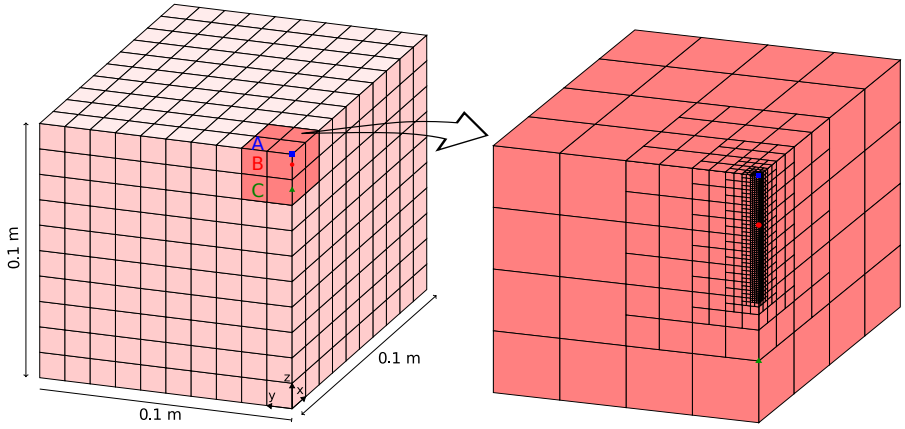

Figure 8: (Left) Computational model (Ω_0) of a quarter of the tissue. **B** (red circle), (0, 0, 0.096), is the injection point, **A** (blue square), (0, 0, 0.1), and **C** (green triangle), (0, 0, 0.085), are observation points. (Right) Zoom-in of the refinement region (shown in dark red region on the left) near the injection site, **B**.

reference configuration using the pull-back operation, as follows

$$\int_0^T \int_{\Omega_t} \hat{q}_f(\boldsymbol{x}, t) \mathrm{d}\Omega_t \mathrm{d}t = \boldsymbol{\chi}_{\Omega_e^{\mathbf{B}}} \int_0^T Q_f(t) \mathrm{d}t, \tag{44}$$

where $\boldsymbol{\chi}_{\Omega_e^{\mathbf{B}}}$ is the indicator function over $\Omega_e^{\mathbf{B}} \in \mathcal{T}_h$, which is the element in the triangulation such that $\mathbf{B} \in \Omega_e^{\mathbf{B}}$ (**B** is shown on the left of fig. 8), and $Q_f(t)$ is shown in fig. 9. The total injected drug is 1.98 mL (0.495 mL for the quarter domain) over a duration of 5 s with an average injection rate of 0.4 mL/s. In practice, self-administration of mAbs (1 - 2 mL) completes within seconds [2, 7, 31, 37, 48], thus the injection rate we have used is clinically relevant.

5.2. Comparison between the poro-viscoelastic and poro-hyperelastic models

We apply both the poro-viscoelastic and poro-hyperelastic models to study the subcutaneous injection. For the viscoelastic relation, we use the constitutive parameters presented in table 1. For the hyperelastic model, we also extract the constitutive parameters from table 1 but use only the one-term Ogden hyperelastic model parameters. Then the Lamé constants are obtained through $\lambda = 2\mu\nu/(1-2\nu)$, where μ is obtained using eq. (21). In addition, we choose the Poisson ratio $\nu = 0.49$, initial permeability $k_0 = 5$ D , and initial porosity $\phi_{f,0} = 0.1$.

The comparisons of the pore pressure at the injection site **B** and observation point **C**, vertical displacement at the skin surface **A**, and the Jacobian determinant in the L^∞ norm of the tissue using the poro-viscoelastic and poro-hyperelastic models are presented in fig. 10. The location of the observation

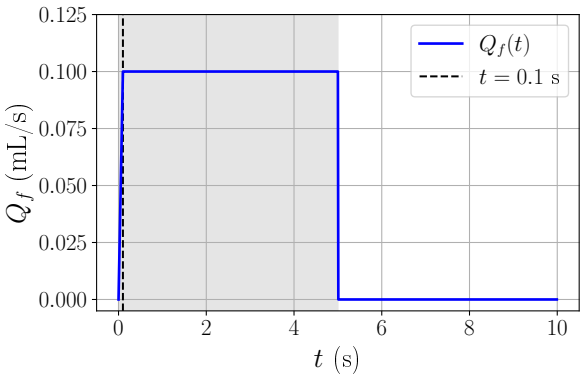

Figure 9: Volumetric injection rate ($Q_f(t)$) over time. The shaded area represents the injection process.

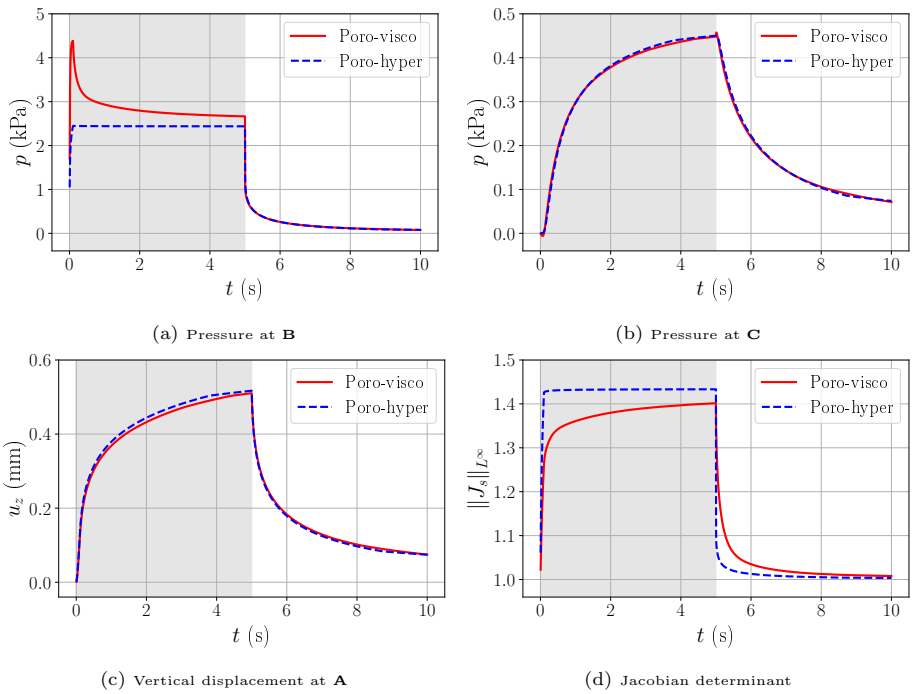

(a) Pressure at **B**

(b) Pressure at **C**

(c) Vertical displacement at **A**

(d) Jacobian determinant

Figure 10: Comparison of the pressure, displacement, and the Jacobian determinant for the poro-viscoelastic (poro-visco in the legend) and poro-hyperelastic (poro-hyper in the legend) models. The location of the **A, B** and **C** are denoted in fig. 8.

sites are shown in fig. 8.

The pressure profiles at the injection site differ significantly during the injection process, see fig. 10a. The pressure at the injection site increases to significant values at the beginning of the injection for both models. As more fluid is injected, the pressure decreases for the poro-viscoelastic model, while that of the poro-hyperelastic model stays flat. At the end of the injection, both models predict a large pressure drop at the injection site, and the pressure predictions of the two models overlap beyond the end of the injection.

As shown in figs. 10b and 10c, the pressure profiles at **C** and the vertical displacement profiles at **A** of the two models are similar. The trends of the maximum Jacobian determinant presented in fig. 10d are in good agreement for the two models, even though the poro-hyperelastic model predicts larger deformation than the poro-viscoelastic model. Results in fig. 10d confirm that the tissue deformation, due to subcutaneous injection, is so large that the use of the nonlinear poro-elastic model is necessary.

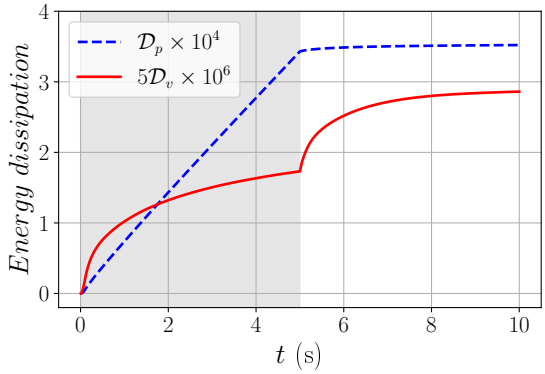

Figure 11: The scaled energy dissipation of the poro-viscoelastic model.

The viscous and porous dissipation are scaled by different constants and presented in fig. 11. Contrary to the relaxation test in section 4, the viscous dissipation is much smaller than the porous dissipation for the subcutaneous injection. At the beginning and the end of the injection when the injection rate changes, the viscous dissipation increases sharply.

We conclude that the viscosity effect of the solid is important in predicting the pressure at the injection site, while the Ogden hyperelastic model is enough to characterize the tissue deformation away from the injection site.

The pressure at the injection site is an important measurement in the injection physiology, and one that has received significant attention in experimental studies [16], because the pore pressure is critical in determining if fractures will be initiated in the tissue due to injection [12]. We remark that the general trend of the pressure profile at the injection site (fig. 10a) resembles the experimental data presented in [16, fig.4a], but differs from others, such as [16, fig.4b and 4c]. This may be due to the difference of the instant injection rates between

the simulation and the experiments. The time evolution of the injection rates in [16] is unknown and is difficult to measure. The reported flow rates in [16] are average values. To improve the simulation, it is necessary to use realistic instant injection rate.

6. Conclusion

In this work, we have used a poro-viscoelastic model to study the injection of mAbs into subcutaneous tissue. First, we validated the model by simulating the relaxation test conducted in [10]. The constitutive parameters of the viscoelastic model are taken from the experiments. Numerical results using the hyperelastic, viscoelastic, poro-hyperelastic and poro-viscoelastic models are compared with one set of the experiments and against each other. The Cauchy stresses obtained from the viscoelastic and poro-viscoelastic models are similar and are in good agreement with experimental data. Moreover, the viscous dissipation is much larger than the porous dissipation of the relaxation test. The hyperelastic and poro-hyperelastic models are not suitable to describe the relaxation behaviour of the adipose tissue.

Next, we applied the poro-viscoelastic model to study the subcutaneous injection utilizing the computational framework developed in [33]. By comparing simulation results of the poro-viscoelastic model with the poro-hyperelastic model adopted in [33], we found that the pressure profiles at the injection site differ significantly for the two models during the injection process. The pressure at the injection site is of great significance because it can indicate if fractures will be initiated in the tissue. After an initial rise, the pressure at the injection site of the poro-viscoelastic model declines, while that of the poro-hyperelastic model stays flat. At locations away from the injection site, the pressure and vertical displacement profiles obtained using the two models are similar. In terms of energy dissipation of the subcutaneous injection, the porous dissipation plays the dominant role. We came to the conclusion that the viscosity effect of the solid is important in predicting the pressure at the injection site, while the hyperelastic model is enough to capture the behaviour of the subcutaneous tissue away from the injection site.

This is the fourth work of modeling subcutaneous injection using poroelasticity and there are many challenging problems unsolved. The time evolution of the injection rate adopted here is only a simple characterization of the subcutaneous injection. A detailed study of the injection rate is suggested so as to improve the simulations. Permeability values reported in experiments differ in several orders of magnitude [12, 24, 32, 43, 54]. In this and previous works [33], the minimum initial permeability (k_0) studied is 0.5 D. This is due to the limitation that further reducing the permeability results in negative Jacobian determinant which violates the constitutive relation of the solid. Changing the solid constitutive law from hyperelasticity to viscoelasticity does not overcome such limitation, so it is worthwhile to use other variable permeability models [49], and to study possible fractures initiated due to injection [12]. Moreover, the computational cost is demanding for nonlinear poro-elastic models. Large

deformation only takes place near the injection site and linear poro-elastic model is still valid away from the injection site [33]. One way to make computations more efficient is to couple linear and nonlinear poro-elasticity together using domain decomposition [23].

Acknowledgements

We greatly appreciate the meaningful discussion with Adrian Buganza, and the helpful comments from the reviewers which lead to significant improvement of the manuscript. This work is partially supported by Eli Lilly and company.

References

[1] Arndt, D., Bangerth, W., Blais, B., Clevenger, T.C., Fehling, M., Grayver, A.V., Heister, T., Heltai, L., Kronbichler, M., Maier, M., Munch, P., Pelteret, J.P., Rastak, R., Thomas, I., Turcksin, B., Wang, Z., Wells, D., 2020. The `deal.II` library, version 9.2. Journal of Numerical Mathematics 28, 131–146. URL: https://dealii.org/deal92-preprint.pdf, doi:10.1515/jnma-2020-0043.

[2] Badkar, A.V., Gandhi, R.B., Davis, S.P., LaBarre, M.J., 2021. Subcutaneous delivery of high-dose/volume biologics: Current status and prospect for future advancements. Drug Design, Development and Therapy 15, 159.

[3] Bangerth, W., Hartmann, R., Kanschat, G., 2007. deal.II – a general purpose object oriented finite element library. ACM Trans. Math. Softw. 33, 24/1–24/27.

[4] Biot, M.A., 1941. General theory of three-dimensional consolidation. Journal of applied physics 12, 155–164.

[5] Biot, M.A., 1956. Theory of propagation of elastic waves in a fluid-saturated porous solid. ii. higher frequency range. The Journal of the acoustical Society of america 28, 179–191.

[6] Biot, M.A., Temple, G., 1972. Theory of finite deformations of porous solids. Indiana University Mathematics Journal 21, 597–620.

[7] Bittner, B., Richter, W., Schmidt, J., 2018. Subcutaneous administration of biotherapeutics: an overview of current challenges and opportunities. BioDrugs 32, 425–440.

[8] Budday, S., Sommer, G., Birkl, C., Langkammer, C., Haybaeck, J., Kohnert, J., Bauer, M., Paulsen, F., Steinmann, P., Kuhl, E., et al., 2017. Mechanical characterization of human brain tissue. Acta biomaterialia 48, 319–340.

[9] Callejas, A., Melchor, J., Faris, I.H., Rus, G., 2020. Hyperelastic ex vivo cervical tissue mechanical characterization. Sensors 20, 4362.

[10] Calvo-Gallego, J.L., Domínguez, J., Cía, T.G., Ciriza, G.G., Martínez-Reina, J., 2018. Comparison of different constitutive models to characterize the viscoelastic properties of human abdominal adipose tissue. a pilot study. Journal of the mechanical behavior of biomedical materials 80, 293–302.

[11] Comellas, E., Budday, S., Pelteret, J.P., Holzapfel, G.A., Steinmann, P., 2020. Modeling the porous and viscous responses of human brain tissue behavior. Computer Methods in Applied Mechanics and Engineering 369, 113128.

[12] Comley, K., Fleck, N., 2011. Deep penetration and liquid injection into adipose tissue. Journal of Mechanics of Materials and Structures 6, 127–140.

[13] Comley, K., Fleck, N., 2012. The compressive response of porcine adipose tissue from low to high strain rate. International Journal of Impact Engineering 46, 1–10.

[14] Coussy, O., 2004. Poromechanics. John Wiley & Sons.

[15] Dimitrov, D.S., 2012. Therapeutic proteins, in: Therapeutic Proteins. Springer, pp. 1–26.

[16] Doughty, D.V., Clawson, C.Z., Lambert, W., Subramony, J.A., 2016. Understanding subcutaneous tissue pressure for engineering injection devices for large-volume protein delivery. Journal of pharmaceutical sciences 105, 2105–2113.

[17] Ehlers, W., 2002. Porous media: theory, experiments and numerical applications. Springer Science & Business Media.

[18] Ehlers, W., Eipper, G., 1999. Finite elastic deformations in liquid-saturated and empty porous solids, in: Porous Media: Theory and Experiments. Springer, pp. 179–191.

[19] Ehlers, W., Karajan, N., Markert, B., 2009. An extended biphasic model for charged hydrated tissues with application to the intervertebral disc. Biomechanics and modeling in mechanobiology 8, 233.

[20] Ehlers, W., Wagner, A., 2013. Constitutive and computational aspects in tumor therapies of multiphasic brain tissue, in: Computer Models in Biomechanics. Springer, pp. 263–276.

[21] Ehlers, W., Wagner, A., 2015. Multi-component modelling of human brain tissue: a contribution to the constitutive and computational description of deformation, flow and diffusion processes with application to the invasive drug-delivery problem. Computer methods in biomechanics and biomedical engineering 18, 861–879.

[22] Fornells, P., García-Aznar, J.M., Doblaré, M., 2007. A finite element dual porosity approach to model deformation-induced fluid flow in cortical bone. Annals of biomedical engineering 35, 1687–1698.

[23] Girault, V., Wheeler, M.F., Almani, T., Dana, S., 2019. A priori error estimates for a discretized poro-elastic–elastic system solved by a fixed-stress algorithm. Oil & Gas Science and Technology–Revue d'IFP Energies nouvelles 74, 24.

[24] Guyton, A.C., Scheel, K., Murphree, D., 1966. Interstitial fluid pressure: Iii. its effect on resistance to tissue fluid mobility. Circulation Research 19, 412–419.

[25] Haller, M.F., 2007. Converting intravenous dosing to subcutaneous dosing with recombinant human hyaluronidase. Pharm Tech 31, 861–864.

[26] Hirsch, S., 2018. A biphasic poroelasticity model for soft tissue, in: Quantification of Biophysical Parameters in Medical Imaging. Springer, pp. 71–88.

[27] Holzapfel, G.A., 2002. Nonlinear solid mechanics: a continuum approach for engineering science. Meccanica 37, 489–490.

[28] Holzapfel, G.A., Ogden, R.W., 2017. Biomechanics: trends in modeling and simulation. volume 316. Springer.

[29] J-P. V., P., 2017. The deal.ii code gallery: Quasi-static finite-strain quasi-incompressible visco-elasticity. doi:10.5281/zenodo.437604.

[30] Jackisch, C., Müller, V., Maintz, C., Hell, S., Ataseven, B., 2014. Subcutaneous administration of monoclonal antibodies in oncology. Geburtshilfe und Frauenheilkunde 74, 343.

[31] Kang, D., Oh, D., Fu, G., Anderson, J., Zepeda, M., 2013. Porcine model to evaluate local tissue tolerability associated with subcutaneous delivery of protein. Journal of pharmacological and toxicological methods 67, 140–147.

[32] Kim, H., Park, H., Lee, S.J., 2017. Effective method for drug injection into subcutaneous tissue. Scientific reports 7, 1–11.

[33] Leng, Y., de Lucio, M., Gomez, H., 2021. Using poro-elasticity to model the large deformation of tissue during subcutaneous injection. Computer Methods in Applied Mechanics and Engineering 384, 113919.

[34] de Lucio, M., Bures, M., Ardekani, A.M., Vlachos, P.P., Gomez, H., . Isogeometric analysis of subcutaneous injection of monoclonal antibodies. Computer Methods in Applied Mechanics and Engineering 373, 113550.

[35] MacMinn, C.W., Dufresne, E.R., Wettlaufer, J.S., 2016. Large deformations of a soft porous material. Physical Review Applied 5, 044020.

[36] Malandrino, A., Moeendarbary, E., 2019. Poroelasticity of living tissues. Encyclopedia of Biomedical Engineering 2, 238–245.

[37] Mathaes, R., Koulov, A., Joerg, S., Mahler, H.C., 2016. Subcutaneous injection volume of biopharmaceuticals—pushing the boundaries. Journal of pharmaceutical sciences 105, 2255–2259.

[38] Ogden, R.W., 1972. Large deformation isotropic elasticity–on the correlation of theory and experiment for incompressible rubberlike solids. Proceedings of the Royal Society of London. A. Mathematical and Physical Sciences 326, 565–584.

[39] Patel, P.N., Smith, C.K., Patrick Jr, C.W., 2005. Rheological and recovery properties of poly (ethylene glycol) diacrylate hydrogels and human adipose tissue. Journal of Biomedical Materials Research Part A: An Official Journal of The Society for Biomaterials, The Japanese Society for Biomaterials, and The Australian Society for Biomaterials and the Korean Society for Biomaterials 73, 313–319.

[40] Pelteret, J.P., Davydov, D., McBride, A., Vu, D.K., Steinmann, P., 2016. Computational electro-elasticity and magneto-elasticity for quasi-incompressible media immersed in free space. International Journal for Numerical Methods in Engineering 108, 1307–1342.

[41] Porter, C., Edwards, G., Charman, S.A., 2001. Lymphatic transport of proteins after sc injection: implications of animal model selection. Advanced drug delivery reviews 50, 157–171.

[42] Rahimi, E., Aramideh, S., Gomez, H., Ardekani, A., 2021. Utransport and lymphatic uptake of monoclonal antibodies after subcutaneous injection. Submitted .

[43] Reddy, N.P., Cochran, G.V.B., Krouskop, T.A., 1981. Interstitial fluid flow as a factor in decubitus ulcer formation. Journal of Biomechanics 14, 879–881.

[44] de Rooij, R., Kuhl, E., 2016. Constitutive modeling of brain tissue: current perspectives. Applied Mechanics Reviews 68.

[45] Sánchez, M.T., Pérez, M.Á., García-Aznar, J.M., 2020. The role of fluid flow on bone mechanobiology: mathematical modeling and simulation. Computational Geosciences , 1–8.

[46] Shovkun, I., Espinoza, D.N., 2019a. Fracture propagation in heterogeneous porous media: pore-scale implications of mineral dissolution. Rock Mechanics and Rock Engineering 52, 3197–3211.

[47] Shovkun, I., Espinoza, D.N., 2019b. Propagation of toughness-dominated fluid-driven fractures in reactive porous media. International Journal of Rock Mechanics and Mining Sciences 118, 42–51.

[48] Shpilberg, O., Jackisch, C., 2013. Subcutaneous administration of rituximab (mabthera) and trastuzumab (herceptin) using hyaluronidase. British journal of cancer 109, 1556–1561.

[49] Shrestha, P., Stoeber, B., 2020. Imaging fluid injections into soft biological tissue to extract permeability model parameters. Physics of Fluids 32, 011905.

[50] Simon, B.R., 1992. Multiphase poroelastic finite element models for soft tissue structures. Applied Mechanics Reviews 45, 191–218.

[51] Sims, A.M., Stait-Gardner, T., Fong, L., Morley, J.W., Price, W.S., Hoffman, M., Simmons, A., Schindhelm, K., 2010. Elastic and viscoelastic properties of porcine subdermal fat using mri and inverse fea. Biomechanics and modeling in mechanobiology 9, 703–711.

[52] Sommer, G., Eder, M., Kovacs, L., Pathak, H., Bonitz, L., Mueller, C., Regitnig, P., Holzapfel, G.A., 2013. Multiaxial mechanical properties and constitutive modeling of human adipose tissue: a basis for preoperative simulations in plastic and reconstructive surgery. Acta biomaterialia 9, 9036–9048.

[53] Sun, Z., Lee, S.H., Gepner, B.D., Rigby, J., Hallman, J.J., Kerrigan, J.R., 2021. Comparison of porcine and human adipose tissue loading responses under dynamic compression and shear: A pilot study. Journal of the Mechanical Behavior of Biomedical Materials 113, 104112.

[54] Thomsen, M., Hernandez-Garcia, A., Mathiesen, J., Poulsen, M., Sørensen, D.N., Tarnow, L., Feidenhans, R., 2014. Model study of the pressure buildup during subcutaneous injection. PloS one 9, e104054.

[55] Usach, I., Martinez, R., Festini, T., Peris, J.E., 2019. Subcutaneous injection of drugs: literature review of factors influencing pain sensation at the injection site. Advances in therapy 36, 2986–2996.

[56] Weickenmeier, J., Saez, P., Butler, C., Young, P., Goriely, A., Kuhl, E., 2017. Bulging brains. Journal of Elasticity 129, 197–212.